The Electrochemical Properties of $Sr(Ti,Fe)O_{3-\delta}$ for Anodes in Solid Oxide Fuel Cells

Andreas Nenning,[a,z] Lukas Volgger,[b] Elizabeth Miller,[c] Liliana V. Mogni,[d] Scott Barnett,[c,*] and Jürgen Fleig[b,*]

[a]*Department of Materials, ETH Zurich, Zurich, 8049 Switzerland*
[b]*Institute of Chemical Technologies and Analytics, Vienna University of Technology, Vienna A-1060, Austria*
[c]*Department of Materials Science and Engineering, Northwestern University, Evanston, Illinois 60208, USA*
[d]*Departamento Caracterización de Materiales- Centro Atómico Bariloche, CP 8400, S. C. de Bariloche, Argentina*

Reduction-stable mixed ionic and electronic conductors such as $Sr(Ti,Fe)O_{3-\delta}$ (STF) are promising materials for application in anodes of solid oxide fuel cells. The defect chemistry of STF and its properties as solid oxide fuel cell (SOFC) cathode have been studied thoroughly, while mechanistic investigations of its electrochemical properties as SOFC anode material are still scarce. In this study, thin film model electrodes of STF with 30% and 70% Fe content were investigated in H_2+H_2O atmosphere by electrochemical impedance spectroscopy. Lithographically patterned thin film Pt current collectors were applied on top or beneath the STF thin films to compensate for the low electronic conductivity under reducing conditions. Oxygen exchange resistances, electronic and ionic conductivities and chemical capacitances were quantified and discussed in a defect chemical model. Increasing Fe content increases the electro-catalytic activity of the STF surface as well as the electronic and ionic conductivity. Current collectors on top also increase the electrochemical activity due to a highly active Pt-atmosphere-STF triple phase boundary. Furthermore, the electrochemical activity depends decisively on the H_2:H_2O mixing ratio and the polarization. Fe^0 nanoparticles may evolve on the surface in hydrogen rich atmospheres and increase the hydrogen adsorption rate.

Manuscript submitted November 28, 2016; revised manuscript received February 8, 2017. Published February 18, 2017.

Acceptor-doped mixed ionic and electronic conductors are a promising class of materials for application in solid oxide fuel cell (SOFC) electrodes and they are widely investigated as SOFC cathodes due to their low polarization resistance.[1–3] Some of these materials are chemically stable and mixed conducting also in humidified hydrogen atmosphere,[4] which makes them applicable in SOFC anodes. Several mixed conductors, such as acceptor doped $(La,Sr)(Cr,Mn)O_3$,[5–8] donor-doped $SrTiO_3$[9,10] and $Sr(Ti,Fe)O_{3-\delta}$-$Ce_{0.9}Gd_{0.1}O_{2-\delta}$ (STF-GDC) composites[11] were investigated in form of porous SOFC anodes. Most of these studies revealed moderately low polarization resistances. In STF-GDC composites, for example, the anode polarization resistance was $<0.2\ \Omega\ cm^2$ at 800°C, and the overall performance increased with increasing Fe content. However, the usually ill-defined geometry of porous electrodes makes the analysis of specific materials parameters such as electronic and ionic conductivity or oxygen exchange activity very challenging.

Thin film model electrodes have well defined and controllable geometry and comparatively simple pathways of electron and oxygen ion migration. This strongly facilitates identification of reaction pathways and quantification of the oxygen exchange activity of the material's surface.[12–18] Mechanistic studies using thin film model electrodes have so far been performed mainly in oxidizing atmosphere. Thorough studies of the mechanisms of electrochemical oxygen exchange in reducing atmospheres are still largely missing, not only for STF, but for most reduction stable mixed conductors, except for (Gd or Sm) doped ceria[19–24] and a study on $(La,Sr)FeO_{3-\delta}$.[25] The typically low electronic conductivity of acceptor doped oxides in reducing atmosphere requires current collectors added to the thin film electrodes. Recently, a special electrode and current collector geometry was thus developed for investigating such weakly electron conducting materials.[4] Fitting of the impedance spectra to a proper equivalent circuit model enabled separation of resistive contributions from the surface reaction and in-plane charge transport. The circuit model proposes that electrochemically driven oxygen exchange is only possible within a characteristic distance (L_C) from the current collectors and indeed this could be visualized by ^{18}O isotope exchange.[26]

In this study, the electrochemical properties of thin film electrodes of STF with an Fe content of 30% and 70% were investigated in H_2+H_2O atmosphere. STF is a well suited model material because of its high thermo-chemical stability and the good knowledge of its electrochemical properties in oxidizing atmospheres.[17,27–32] Lithographically patterned Pt current collectors were applied beneath the STF thin films to compensate the comparatively low electronic conductivity in reducing conditions.[4,32] Pt current collectors on top were tested as well and a high electro-catalytic activity was observed at the Pt-STF-atmosphere triple phase boundary. Also increased electronic and ionic conductivity and decreased polarization resistance were found on electrodes with higher Fe content. This trend is in line with various studies investigating STF-based SOFC cathodes. Moreover, atmosphere and DC bias were varied to trigger the exsolution of Fe^0 particles, which may catalyze the surface reaction.[33,34]

Experimental

Thin film electrodes of $SrTi_{0.3}Fe_{0.7}O_{3-\delta}$ (STF37) and $SrTi_{0.7}Fe_{0.3}O_{3-\delta}$ (STF73) were prepared by pulsed laser deposition (PLD) using a KrF excimer laser (Lambda COMPexPro 201F, 248 nm wavelength). Deposition was performed at 650°C substrate temperature with the laser operating at 400 mJ, 5 Hz for 30 minutes, resulting in a final film thickness of approx. 120 nm for STF37 and 170 nm for STF73. Either [100] oriented 9.5 mol% Y_2O_3 doped zirconia (YSZ) single crystals or [100] oriented MgO single crystals were used as substrates. The target powders were prepared via solid state reaction of appropriately weighed $SrCO_3$, Fe_2O_3 and TiO_2 powders and the pressed targets were sintered in air at 1400°C.

Micro-patterned current collectors, consisting of 75 nm sputtered Pt and ~5 nm Ti adhesion layer, were either deposited on top of the STF film or embedded between substrate and STF and structured by photolithographic methods. Ar ion beam milling was used to structure the embedded current collectors and STF layer, and lift-off processing was used for structuring the top current collector, to avoid sputtering damage on the STF surface. Visible in the scanning electron microscopy (SEM) images in Figure 1d the edges of the top current collector are bent upwards as an artefact from the unidirectional sputter deposition of Pt. This artefact only occurs for the lift-off technique. The various resulting sample geometries are summarized in Figure 1.

Samples with microelectrodes.—Microelectrodes were fabricated by photolithographic micro-structuring from STF thin films with

*Electrochemical Society Member.
[z]E-mail: andreas.nenning@mat.ethz.ch

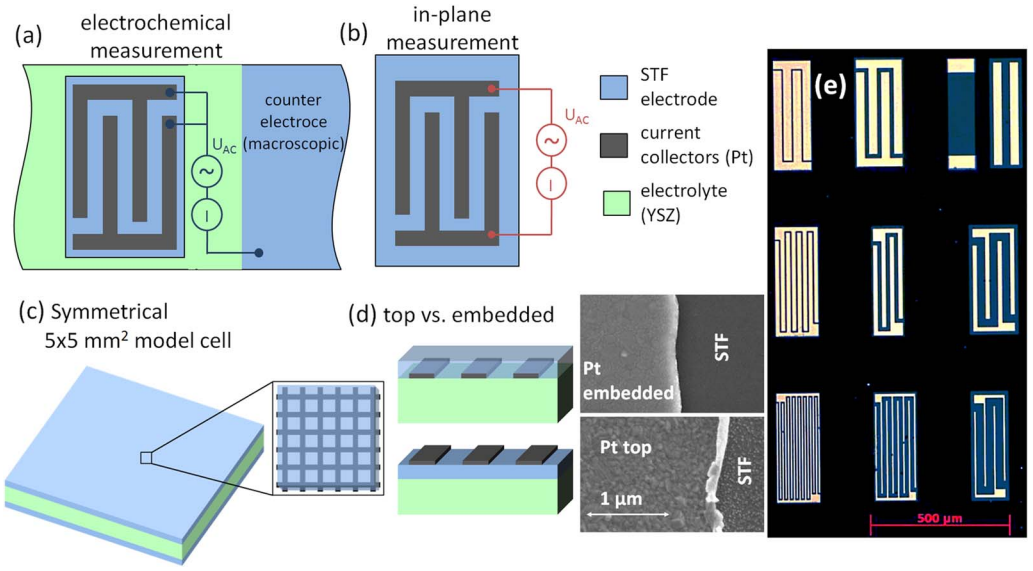

Figure 1. Types of investigated samples: (a) Microelectrode on YSZ, with current collectors in electrochemical contacting mode. (b) Continuous STF thin film on MgO with embedded current collectors for in-plane conductivity measurements. (c) Symmetrical 5 × 5 mm^2 cell with macroscopic electrodes and embedded current collector grid used for temperature-dependent measurements. (d) Sketch and SEM images of thin films with top and embedded current collectors. (e) Micrograph of microelectrodes with the nine investigated current collector geometries.

current collectors, deposited on polished 10∗10∗0.5 mm^3 YSZ substrates. A 30 mm^2 large electrode of the same STF film with current collectors was used as counter electrode. Owing to its much larger size it did not affect the measured impedance spectra. Each microelectrode contains two current collectors, as shown in Figure 1a. In the electrochemical contacting mode the entire microelectrode is polarized against the larger counter electrode. Equivalent circuit models for such microelectrodes were derived in Ref. 4. The width and distance between the current collecting fingers were both varied between 5, 15 and 30 µm, resulting in the 9 different current collector geometries shown in Figure 1e. Microelectrodes of all 9 geometries were investigated in an asymmetrically heated, gastight micro-contact measurement chamber using gold-plated steel contact tips. A ceramic heating stage (Linkam TMS 1000) was employed to heat the samples up to ∼650°C sample temperature in humidified Ar-H_2 (Alphagaz Arcal 10), containing 25 mbar H_2 and ca. 18 mbar H_2O. Furthermore, such samples were characterized in a tube furnace micro contact setup with precisely controlled, homogeneous temperature[35] in varying H_2:H_2O mixing ratio.

STF thin films on MgO substrates.—STF thin films on MgO substrates were used for in-plane conductictivity measurements and fabricated similarly to the samples with microelectrodes and embedded current collectors, only structuring of the STF layer was omitted, because the in-plane current is anyway restricted to the region between the current collecting fingers sketched in Figure 1b. These sampes were characterized by impedance spectroscopy in a homogeneously heated tube furnace setup at 650°C under varying H_2:H_2O mixing ratio. An optimized contacting stage with two moveable contact tips was used to contact both interdigitating current collectors.

Symmetrical samples with 'macroscopic' electrodes.—Symmetrical samples with 'macroscopic' electrodes were prepared by deposition of STF electrodes with embedded current collectors on both sides of YSZ substrates, as sketched in Figure 1c. Sample dimensions were 5 × 5 × 0.5 mm^3 and the current collector was fabricated as a fine structured grid (4 µm stripes, 11 × 11 $µm^2$ open space). Also these samples were measured in a homogeneously heated tube furnace setup in a temperature range of 350–800°C, using humidified Ar-H_2 mixture (25 mbar H_2, 25 mbar H_2O).

All impedance measurements were performed with a Novocontrol Alpha-A impedance analyzer at 10 mV RMS.

Thermogravimetric analysis (TGA).—The oxygen non-stoichiometry of STF37 sample was determined at 650°C by thermogravimetric analysis (TGA). The powder for TGA was produced by the same solid state reaction as the PLD targets, except for a lower firing temperature of 1200°C for 1 h in air to avoid excessive sintering. A highly sensitive thermogravimetric equipment consisting of a symmetrical thermobalance based on a Cahn 1000 electrobalance coupled to a ZrO_2-based oxygen pump and sensor system[36] was used, which allows determination of sample mass changes within ±10 µg with 0.6 g of STF37 powder. The oxygen partial pressure (pO_2) was varied between 10^{-25} and 1 bar by using O_2-Ar and H_2-H_2O mixtures. For quantification of the oxygen content, the plateau in the isotherm of mass vs pO_2 was used. This plateau corresponds to full Fe^{3+} formation, meaning 3-δ = 2.65 for 70% Fe doped STF, and it is a common feature of Fe containing perovskites.[37,38]

Results and Discussion

In-plane conductivity of STF.—The electronic and ionic in-plane conductivity of STF37 and STF73 thin films on insulating magnesia substrates was investigated by impedance spectroscopy, using the interdigitating embedded current collectors sketched in Figure 1b. The impedance spectra were measured at 650°C in different H_2:H_2O mixtures, corresponding to a pO_2 range of about 10^{-21} to 10^{-25} bar. A typical spectrum recorded on STF37 is shown in Figure 2 (circles). It consists of the onset of a distorted high frequency arc (not considered in the fit), and a well separated low frequency feature. The latter deviates from an ideal semicircle, partly resembling a 45° Warburg type impedance, indicative of a diffusive process. Hence, two real axis intercepts are found, one at higher frequencies (denoted AC resistance R_{AC}) and one at low frequencies (DC resistance R_{DC}).

Additional variation of the finger distance (between 5 and 30 µm) revealed a linear increase of the measured AC and DC resistances with finger distance. This shows that in-plane conduction processes in the STF film are predominant while surface exchange processes have a negligible impact. In such a case, the high frequency axis intercept corresponds to the total conductivity, while the DC resistance reflects

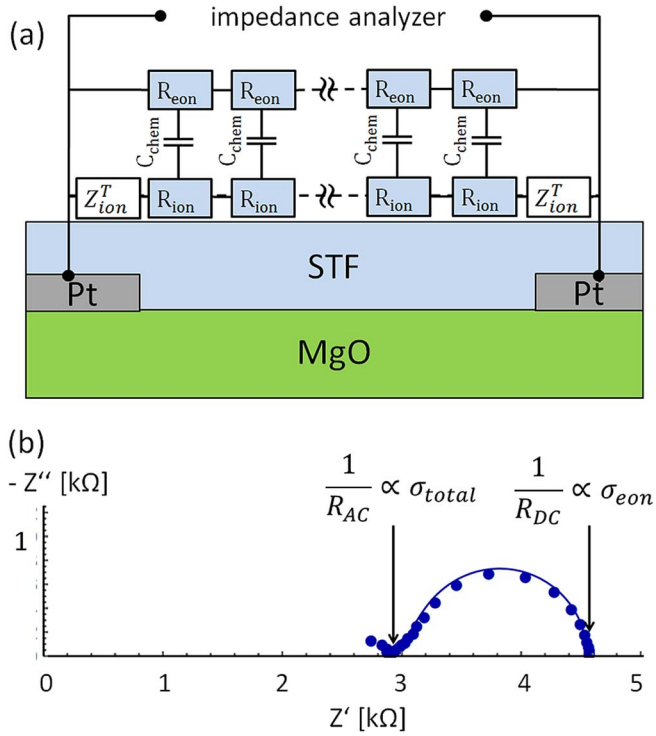

Figure 2. (a) Transmission line equivalent circuit used to fit the in-plane measurements on MgO substrates. (b) Impedance spectrum (circles) and fit (solid line) of an in-plane measurement of STF37 at 650°C.

the electronic conductivity only, due to the ion blocking electrodes. This very simple first analysis, also sketched in Figure 2b, yields essentially the same conductivity values as fitting to the impedance model discussed in the following. Fitting the data to the circuit model shown in Figure 2a helps validating the interpretation by also considering the shape of the low frequency arc and furthermore reveals information on capacitances.

This circuit model for a mixed conducting film on an insulating substrate consists of a transmission line with an ionic (ion) and an electronic (eon) rail, which are coupled via chemical capacitors. This circuit model and its analytic impedance function were derived in Ref. 23, with electronic and ionic terminal impedances still to be specified. Electrons can be reversibly exchanged between STF and current collector, which is treated by a short circuit. Oxygen ions, on the other hand, cannot be exchanged at the current collector interface. The typical treatment of an (ion) blocking electrode would be a capacitor in the ionic rail. However, in our specific case the current collectors are in parallel to the thin film plane. Hence also in-plane migration of oxygen ions on top of the current collector may take place. This is modelled by an open Warburg impedance as terminating element with the impedance function

$$Z^T_{ion} = R_{ion} * \frac{\coth\left(\frac{w_{finger}}{2}\sqrt{i\omega C_{chem} R_{ion}}\right)}{\sqrt{i\omega C_{chem} R_{ion}}} . \qquad [1]$$

R_{ion} is the ionic sheet resistance (resistivity divided by film thickness), C_{chem} the area-specific chemical capacitance and w_{finger} the width of the current collecting finger. Although the analytical impedance function of the circuit model in Figure 2a with Z^T_{ion} from Eq. 1 is rather complex,[23] it includes only three fit parameters (ionic and electronic conductivity, and chemical capacitance), provided the in-plane ionic conductivity and chemical capacitance of the thin film is assumed independent of the substrate (current collector or MgO). Fitting of the in-plane impedance spectra to this equivalent circuit model (performed by minimizing the sum of squared relative errors using

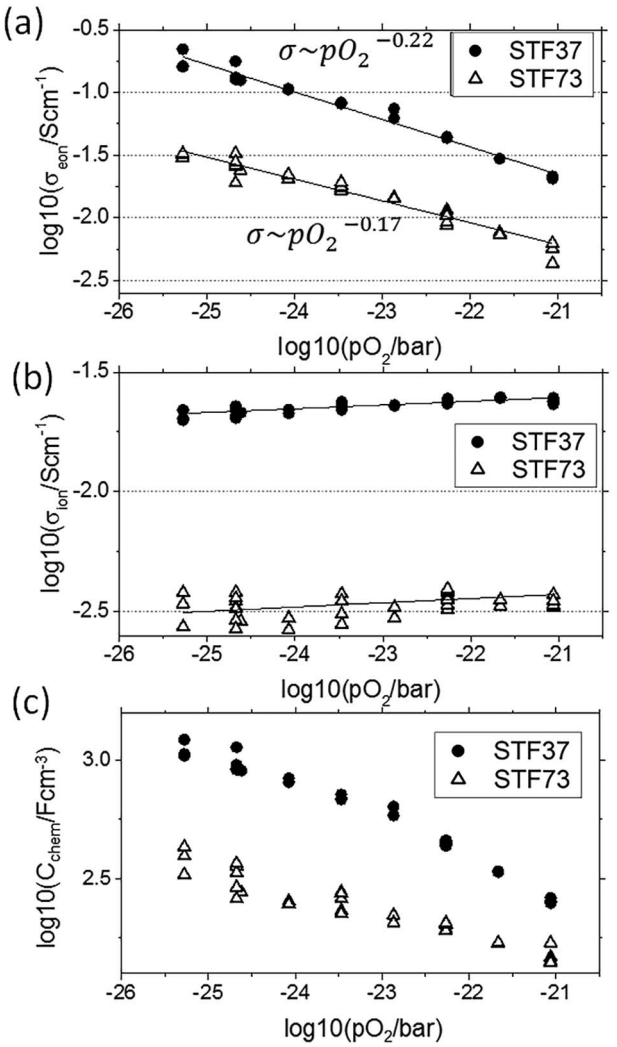

Figure 3. Fit results of the in-plane impedance spectra sketched in Figure 2: Electronic conductivity (a), ionic conductivity (b) and chemical capacitance (c) of STF37 and STF73 at 650°C in varying H_2:H_2O mixing ratio, plotted as a function of pO_2.

Mathematica) yielded the conductivities and capacitances shown in Figure 3 with very small fitting errors.

The results are discussed in terms of the following point defect model for STF:[30,32,38] Electronic and ionic conductivity as well as chemical capacitance are governed by the concentrations and mobilities of oxygen vacancies ($V_O^{\cdot\cdot}$) and electronic defects. The latter correspond to different oxidation states of Fe, namely Fe^{2+}(Fe''_{Ti}) and Fe^{3+}(Fe'_{Ti}). The concentration of electron holes (formally $Fe^{4+} = Fe^{\times}_{Ti}$) is negligible in reducing atmospheres. The results presented here, as well as XPS[34] and thermogravimetric measurements[38] support the treatment of electronic defect states as localized point defects, rather than as electrons in a conduction band.

In the low pO_2 regime, Fe in STF is mainly present as Fe^{3+}, and the defect charge is largely compensated by oxygen vacancies, making them the majority charge carrier with a concentration $[V_O^{\cdot\cdot}] \approx 0.5[Fe_{Ti}]$. In this defect regime, the concentration of 'electrons' $[Fe''_{Ti}]$ as the minority charge carrier should have a simple dependence on pO_2 according to

$$\left[Fe''_{Ti}\right] \sim pO_2^{-\frac{1}{4}}. \qquad [2]$$

Most likely, a Fe''_{Ti} polaron hopping mechanism causes the electron conductivity (σ_{eon}). Hence, also the electronic conductivity, which

is expected to be proportional to the Fe''_{Ti} concentration should exhibit a $pO_2^{-0.25}$ dependence. Moreover, the chemical capacitance per cm^3 is expected to be proportional to $[Fe''_{Ti}]$ via the relation[39]

$$C_{chem} = \frac{e^2}{k_b T}\left[Fe''_{Ti}\right], \quad [3]$$

where e is the elementary charge and k_b Boltzmann's constant. The atmospheric oxygen partial pressure (pO_2) can be varied via variation of the H_2:H_2O mixing ratio and calculated by the mass action law

$$H_2 + \frac{1}{2}O_2 \rightleftharpoons H_2O, \quad pO_2 = \left(\frac{pH_2O}{pH_2}\right)^2 e^{-\frac{\Delta_r G^0}{k_b T}}. \quad [4]$$

Here, $\Delta_r G^0$ is the Gibbs free energy of hydrogen oxidation at standard pressure.[40] Already here we note that the effective pO_2 in the electrode bulk can also be varied by application of an overpotential. According to Nernst's equation we get for surface limited oxygen exchange kinetics

$$pO_2^{eff} = pO_2 e^{\frac{4e\eta}{k_b T}}, \quad [5]$$

The overpotential η of the electrode is calculated from the applied potential by subtracting resistive losses within the electrolyte. Due to the microelectrode arrangement, overpotential losses in the much larger counter electrode are negligible. In line with the presented defect chemical model, the measured ionic conductivity plotted in Figure 3b is (within experimental error) independent of pO_2, and for STF37 it even exceeds the conductivity of the single crystalline 9.5 mol% Y_2O_3 doped YSZ substrates used in this study (0.022 vs 0.009 Scm^{-1} at 650°C). Oxygen vacancy diffusivities can be calculated by the relation $D_{V_O} = \sigma_{ion} k_b T/(4e^2 c_{V_O})$, with the vacancy concentration c_{V_O} being one half of the Fe concentration. We find $1.8*10^{-7}$ cm^2/s and $4.8*10^{-7}$ cm^2/s for STF73 and STF37, respectively. These values are lower than those typically reported for only slightly doped $SrTiO_3$[43] (between $2*10^{-6}$ and $9*10^{-6}$ cm^2/s at 650°C). This is most probably due to defect interaction which lowers the mobility with increasing defect concentration. However, D_{V_O} is close to the values found in other good oxide ion conductors with high vacancy concentration, such as the YSZ substrates used here ($5.5*10^{-7}$ cm^2/s), or 20% Gd-doped ceria[42] ($1.3*10^{-6}$ cm^2/s). The measured increase of the vacancy mobility with higher Fe concentration might be surprising at first sight; in highly doped zirconia or ceria, for example, the vacancy mobility decreases with increasing doping concentration.[41,42] This effect of high Fe concentration in STF is most likely caused by the dependence of the migration barriers of a vacancy jump on the specific nearest neighbor cation configuration, with Fe presumably lowering this barrier.

Figure 3a shows the electronic conductivity for STF37. The increase of conductivity for lower pO_2 is in agreement with the defect model discussed above, but the slopes are slightly flatter than expected from the model: $\sigma_{eon} \sim pO_2^{-0.22}$ is found for STF37 and $\sigma_{eon} \sim pO_2^{-0.17}$ for STF73. These differences may be caused by defect-defect interactions. The total conductivity of the measurements presented here (including the slightly flatter slopes) also matches the (total) conductivity vs. pO_2 curves of sintered STF[32] pellets with similar Fe content, when the slightly different temperature (750 vs 650°C) is accounted for.

Also the chemical capacitance (Figure 3c) qualitatively follows the defect chemical model. However, the fitting values may be not very accurate, especially when the ionic transference number is small and thus the "arc" in the impedance spectrum is very small compared to the high frequency intercept (R_{AC}). A more reliable measurement of the chemical capacitance by fitting impedance spectra in the electrochemical mode is therefore given in section Oxygen partial pressure dependence of Fe oxidation states.

Effect of the current collector placement.—The area-specific resistance (ASR) of the surface reaction was investigated on STF37 microelectrodes with current collectors either on top or beneath the STF thin film, see sketches in Figures 1a, 1d. Exemplary electrochemical impedance spectra of STF37, measured at 650°C in pH_2 = 25 mbar and pH_2O = 18 mbar, are given in Figure 4. The difference in the high frequency offset in Figure 4 is caused by normalization to different electrochemically active areas. Circuit models elaborated in Ref. 4 for different current collector positions may explain the slightly different shape of the two impedance spectra due to different ion conduction paths. The following measurements, however, show that also the mechanism of oxygen exchange depends on the placement of the current collector.

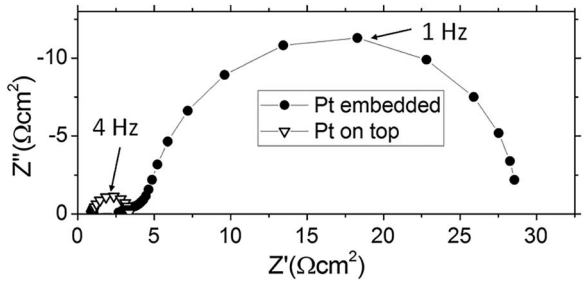

Figure 4. Impedance spectra of STF37 microelectrodes measured at 650°C in the electrochemical mode with current collectors either embedded or on top in pH_2 = 25 mbar and pH_2O = 18 mbar, normalized to the atmoesphere-exposed STF surface area.

When the current collector is placed on top of the electrodes, a part of the STF film is covered by Pt. Mapping of ^{18}O exchange on similar electrodes revealed that the Pt film is not permeable for oxygen and therefore reduces the electrochemically active area of the STF electrode.[26] At the triple phase boundary (TPB), however, the oxygen exchange is catalyzed by the platinum,[42,44] causing the much smaller electrode arc with Pt on top. The contributions of the STF surface and the TPB can be separated by measuring electrodes of all 9 geometries shown in Figure 1e. The area-specific resistances of the electrodes were determined by fitting the dominant low frequency arc of the impedance spectra with a resistor (R_{pol}) in parallel to a constant phase element due to the chemical capacitance (CPE_{chem}) and normalizing the resistance to the atmosphere-exposed STF area. The TPB density was calculated by dividing the circumference of the current collectors (given from the photomask) by the atmosphere-exposed STF area. Although electronic and ionic charge transport may have a significant impact on the impedance of STF thin film electrodes,[4] we can show that R_{pol} measured on the electrodes investigated here is mainly caused by the surface reaction (see below).

When plotting the inverse of this resistance against the TPB density of the electrode, the contributions from different reaction paths (STF surface vs TPB) can be separated by a simple linear regression, see Figure 5. The effect of the TPB density on the electrochemical activity of the surface is very pronounced and a length-specific activity of 0.00014 S/cm or 7000 Ωcm can be estimated. For comparison, Ni-YSZ anodes typically exhibit 10–100 times lower TPB activity[45] at the same temperature.

Recently, isotope exchange[46] on thin film electrodes and electrochemical measurements on porous[47] electrodes showed that the hydrogen oxidation rate on various oxide anodes, including STF37, is limited by hydrogen adsorption. The adsorption limitation is especially important for the conditions used in the present measurements – temperatures below 800°C and relatively low pH_2. It was further shown in Ref. 47 that a catalytic metal on the oxide surface promotes hydrogen dissociative adsorption, with subsequent "spillover" of H atoms from the metal onto the oxide surface. A spillover mechanism can also explain why the 5 nm Ti adhesion layer does not strongly impede the TPB effect. Note that the hydrogen oxidation process at Ni-YSZ TPBs is often modeled using a similar mechanisms with hydrogen spillover from Ni onto YSZ.[48] Superior H_2 dissociation kinetics of Pt and/or a larger active zone for electrochemical reduction of

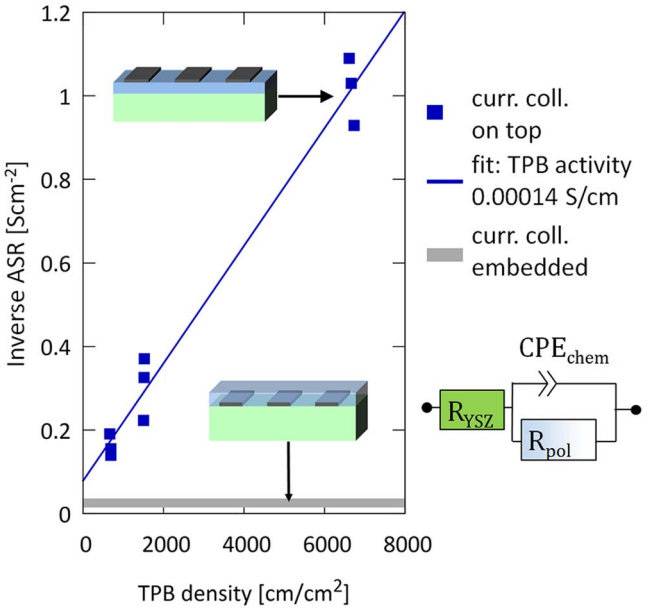

Figure 5. Inverse ASR of STF37 microelectrodes as function of the triple phase boundary (TPB) density (normalized to the atmosphere-exposed STF surface) measured in electrochemical mode at 650°C in $pH_2 = 25$ mbar and $pH_2O = 18$ mbar. ASR values were gained by normalizing R_{pol} to the active surface area. The gray bar on the bottom represents the typical range of inverse ASR measured on electrodes with differently shaped embedded current collectors and thus without TPB.

spillover species can explain the much higher performance of Pt/STF compared to Ni/YSZ TPBs.

On samples with embedded current collectors of different geometries, i.e. electrodes which do not have atmosphere-exposed platinum, the inverse ASR of the two-phase surface reaction is 0.026 ± 0.012 Scm^{-2} (39 ± 20 Ωcm^2). Significant variance of the area-specific resistance even on geometrically identical electrodes on the same substrate causes a comparatively large standard deviation. Statistical errors may be also the reason why the linear fit in Figure 5 does not exactly meet the inverse ASR of STF electrodes with embedded current collectors at zero TPB density.

For embedded current collectors a further data analysis is possible. As elaborated in Ref. 4, the ASR and the in-plane conductivity shown in Figure 3 can be used to calculate the characteristic in-plane charge transport length L_c

$$L_c = \sqrt{d_{STF}\sigma * ASR_{surface}}\,, \qquad [6]$$

where d_{STF} is the thickness of the STF film, and σ is either the electronic (for electronic in-plane charge transport in STF on YSZ), or the ionic (for in-plane ionic charge transport in STF on top of the current collectors). When either the distance or width of the current collectors is larger than L_c, the electrode is not homogeneously active for electrochemical oxygen exchange and the ASR increases, due to limiting in-plane conductivity. Using the conductivity and $ASR_{surface}$ observed in a 1:1 H_2:H_2O mixture for STF37, this length is 25 ± 10 μm for ions and 45 ± 10 μm for electrons. Therefore, in-plane charge transport losses play only a minor role in our study. On electrode geometries with the largest current collector separation and width of 30 μm, in-plane losses may contribute significantly to the total polarization resistance, but the abovementioned strong ASR scatter even on geometrically identical electrodes prevails a clear identification or disproof of this effect.

Temperature dependence of the oxygen exchange kinetics.—The temperature dependence of the area-specific resistance of the surface reaction was investigated in more detail using symmetrical model cells with "macroscopic" 5×5 mm^2 model electrodes, as sketched

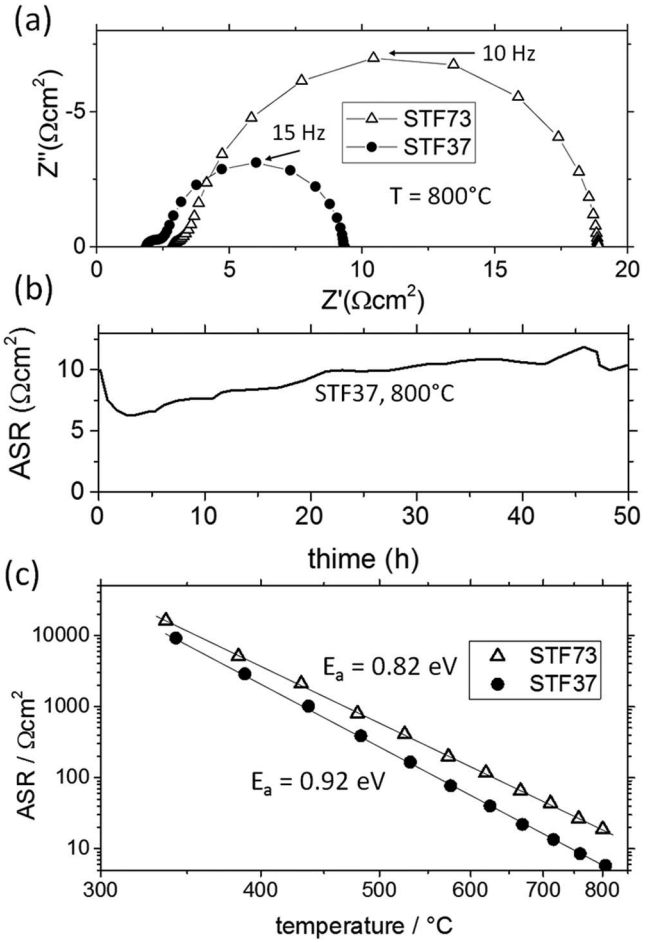

Figure 6. (a) Impedance spectra recorded at 800°C on macroscopic symmetrical cells with 30 and 70% Fe doped STF electrodes in 25 mbar $H_2 + 25$ mbar H_2O. (b) Typical time dependence of the ASR of STF37. (c) Arrhenius plot of the ASR for such measurements.

Figure 1c. A TPB-free, embedded current collector grid with small feature size (11×11 μm^2 holes and 4 μm stripes) was used to ensure homogeneous polarization of the entire STF film and negligible in-plane charge transport resistances due to the small in-plane length scales. Hence, the diameter of the electrode arc seen in Figure 6a is a measure for the ASR, which is relatively stable over time, as shown in Figure 6b. Temperature dependent measurements in 25 mbar $H_2 + 25$ mbar H_2O therefore deliver reliable values for the activation energy of the ASR. At 800°C the ASR of STF37 is roughly half as large as for STF73, see Figure 6a. The better performance for higher Fe content is in line with studies using STF as a cathode material[17] and studies using porous STF-GDC composite anodes.[11] Activation energies extracted from the Arrhenius plots in Figure 6c are below 1 eV in both cases (0.82 eV on STF73 and 0.92 eV on STF37). Such values are in the range of other mixed conducting hydrogen electrode materials, such as ceria,[49,50] but they are very low, compared to the activation energy of O_2 reduction reaction on STF (nearly 2 eV[17]). This difference highlights the mechanistic difference between oxidizing and reducing oxygen exchange.

These results can be compared with recent data from SOFCs with porous STF37 anodes.[47] Although an ASR activation energy was not provided in [Ref.47], the temperature dependence of the ASR values suggests a similar activation energy. The main porous STF37 anode response appears at a few Hz, similar to the value shown here. Finally, the ASR due to oxygen surface exchange at 750°C in Figure 6c, 9 Ωcm^2, can be compared with the ASR of 0.85 Ω cm^2 measured under the conditions in Ref.[47] closest to the present conditions – 750°C,

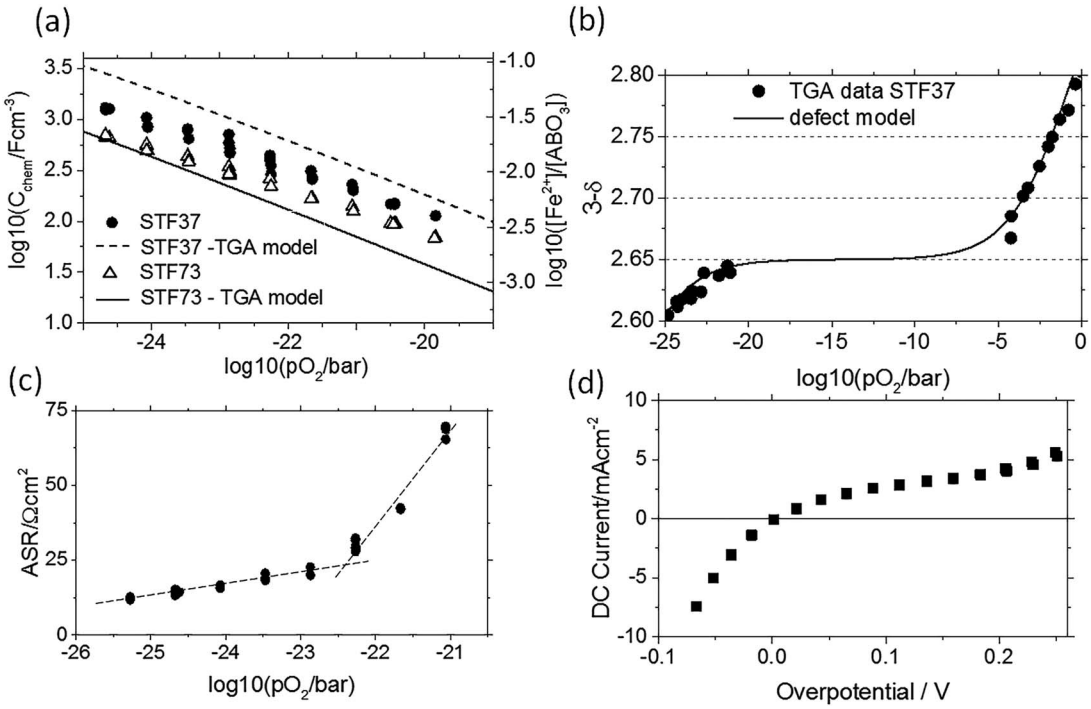

Figure 7. (a) Chemical capacitance and calculated polaron concentration, calculated from electrochemical impedance spectra of STF37 and STF73 at 650°C for different oxygen partial pressures. C_{chem} is linked to $[Fe^{2+}]$ (r.h.s axis) via Eq. 3. Dashed and solid lines result from fitting of TGA data. (b) TGA analysis and fitting of STF37 powder at 650°C. (c) Area specific resistance of STF37 as a function of the atmospheric pO_2. (d) DC characteristics of STF37 measured in hydrogen-rich atmosphere ($pH_2{:}pH_2O = 12{:}1$) at 650°C.

100 mbar H_2, and 30 mbar H_2O. From the electrochemical data of the thin film, the ASR of a porous electrode can be calculated by using a transmission line circuit model[51] and microstructural data from 3D tomography:[47]

$$ASR = \sqrt{\frac{R_{surf}}{\sigma_{ion,eff}\mathrm{a}}}\coth\left(L\sqrt{\frac{\mathrm{a}}{\sigma_{ion,eff}R_{surf}}}\right) \quad [7]$$

In Eq. 7 R_{surf} is the surface-specific oxygen exchange resistance (9 Ωcm^2 according to our thin film measurements), L is the electrode thickness (9 μm), a is the anode surface area (1.6 μm^{-1}), and $\sigma_{ion,eff}$ the STF effective ionic conductivity (the conductivity given in Figure 3, 0.022 S/cm, times the anode solid fraction, 0.77, and divided by the solid-phase tortuosity, 1.1). The resulting ASR value of 0.64 Ω cm^2 is in fair agreement with the porous electrode value in Ref. 47. Although there is significant uncertainty in estimating the effective ionic conductivity of the porous electrode, due to different temperature and microstructure of electrodes in the two types of experiment, this only has minimal impact on the projected ASR, which is mainly caused by the surface reaction ($ASR \approx R_{surf}/aL$).

Oxygen partial pressure dependence of Fe oxidation states.— Further insight into the defect chemistry and thermo-chemical stability of STF was gained from impedance measurements on STF microelectrodes as sketched in Figure 1a. Changing the $H_2{:}H_2O$ mixing ratio at constant total pressure ($pH_2 + pH_2O = 25$ mbar) resulted in an atmospheric oxygen partial pressure range of 10^{-21} to 10^{-25} bar at 650°C. Electrochemical impedance spectra were measured on microelectrodes with a current collector separation of 15 μm (for experiment geometry see Figure 1a) and fitted to the simplified equivalent circuit in Figure 5. The chemical capacitance determined from this fit is plotted in Figure 7a. Chemical capacitance and polaron concentration $[Fe^{2+}]$ on the left and right Y-axes are linked by Eq. 3.

Also thermogravimetric analysis (TGA) can be used to determine a polaron concentration. Thermogravimetric analysis (TGA) of STF37 powder was performed at 650°C. The measured data are shown in Fig. 7b and fitted to the defect chemical model for an acceptor-doped mixed conductor from Ref. 37. The resulting polaron concentration is shon in Fig. 7a (dashed line). Moreover, values determined from TGA literature data for 35% Fe-doped STF[38] are shown (solid line). Even though differences between Fe^{2+} concentrations of STF37 and STF73 are somewhat larger for TGA data, there is good agreement of the absolute values as well as of the pO_2 dependence of thin film chemical capacitance and thermogravimetric data. The moderate mismatch of TGA and impedance-derived nonstoichiometry may be caused by the methodology, but can also originate from the higher density of interfaces in the polycrystalline thin films. We conclude that both methods deliver reliable information on the types and concentrations of electronic and ionic defects.

The mobility of a charge carrier x (μ_x) can be calculated from the conductivity (σ_x) and concentration (c_x) of the charge carrier via $\sigma_x = z_x e \mu_x c_x$. The data plotted in Figure 3a and Figure 7a therefore allows the estimation of the electron mobility. We obtain $\mu_{eon} \approx 6 * 10^{-4} cm^2 V^{-1} s^{-1}$ for STF73 and $\mu_{eon} \approx 1.4 * 10^{-3} cm^2 V^{-1} s^{-1}$ for STF37 at 650°C. These values are only two orders of magnitude larger than the oxygen vacancy mobility at 650°C, calculated from Fig. 3b and $[V_{\ddot{O}}] \approx 0.5[Fe_{Ti}]$ ($\mu_{ion} \approx 4.6 * 10^{-6} cm^2 V^{-1} s^{-1}$ for STF73 and $\mu_{ion} \approx 1.2 * 10^{-5} cm^2 V^{-1} s^{-1}$ for STF37). The rather low mobility of electronic defects supports the model that those are localized to Fe^{2+} ions; this was already suggested by ambient pressure XPS.[34] Most likely, electron transport in STF is similar to the thoroughly investigated Ce^{3+} polaron conduction in ceria, where polaron mobilities are almost the same as for STF.[52–54]

The redox activity of iron also plays an important role for explaining the pO_2 dependence of the surface ASR and the DC characteristics of STF37 electrodes shown in Figures 7c–7d. In a previous ambient-pressure XPS study, the exsolution of Fe^0 on the surface of STF73 and $La_{0.6}Sr_{0.4}FeO_{3-\delta}$ electrodes was observed during cathodic polarization in 1:1 $H_2{:}H_2O$ atmosphere.[34] This Fe0 formation was accompanied by strongly increased electrochemical water splitting kinetics.

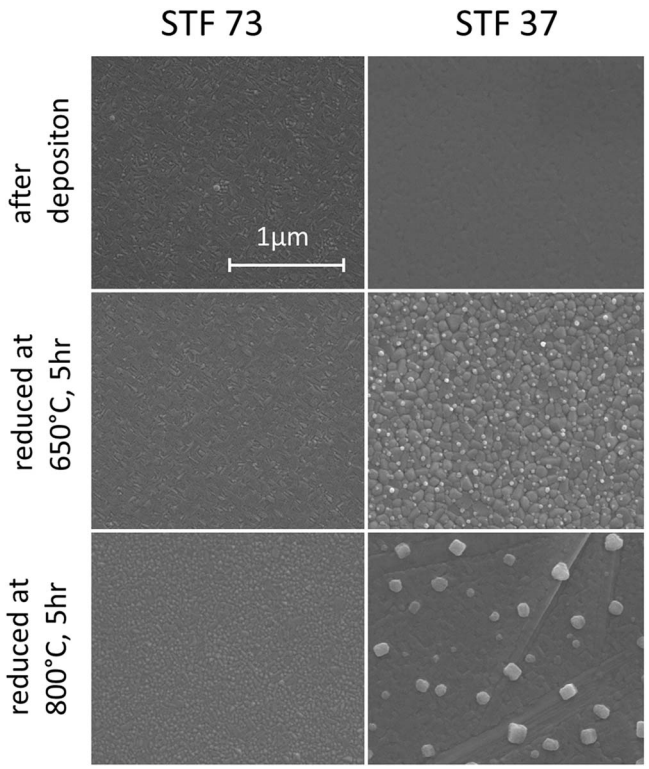

Figure 8. SEM images of STF37 and STF73 before and after reduction at 650°C and 800°C for 5h in 25 mbar H_2+0.8 mbar H_2O.

Improvement of the hydrogen electrode performance by exsolution of easily reducible transition metals was also demonstrated on various (La,Sr)TiO_3 based materials,[9,55,56] (La,Sr)$FeO_{3-\delta}$,[33] (La,Sr)$CrO_{3-\delta}$ based materials,[57–60] and rare earth vanadates.[61] Decreased anode polarization resistance in cells with (La,Sr)(Cr,Ru)$O_{3-\delta}$ anodes was quantitatively modelled by enhanced hydrogen dissociative adsorption at exsolved Ru nanoparticles.[47]

Here, the extent and electrochemical implications of Fe exsolution from STF were further investigated. STF thin films on YSZ were reduced at 650°C or 800°C for 5 hours in 25 mbar H_2 + 0.6 mbar H_2O, which is sufficiently reducing for metallic Fe to be stable compared to Fe oxide.[40] As shown by the SEM images in Figure 8, (metallic) particles can be clearly observed on STF37 after reduction at 650°C. At 800°C, these particles are much larger and the roughening of the remaining STF37 surface even suggests volume decomposition. STF73, on the other hand, appears more stable, and thermally induced Fe exsolution was not observed in SEM.

The exsolved Fe particles are metallic in hydrogen rich atmospheres and become oxidized, or may be again incorporated in the perovskite lattice, in water rich atmospheres. This can explain the change of the slope in the ASR vs log(pO_2) plot and the steeper increase of the ASR in less reducing atmospheres shown in Figure 7c. Such a pronounced change in the pO_2 dependence of the ASR was absent on STF73 (not shown). This is in line with the SEM images in Figure 8, which do not show any evidence for Fe^0 particles. Additionaly, a less reducing atmosphere also implies a smaller H_2 pressure in the atmosphere (the sum of pH_2+pH_2O is kept constant). Since we assume that H_2 adsorption/dissociation, is rate limiting, the low H_2 pressure probably also influences ASR increase in the higher pO_2 regime in Figure 7c.

The catalytic effect of Fe° can also explain the untypical current-voltage characteristics in hydrogen-rich conditions depicted in Figure 7d. Two DC sweeps were recorded at 650°C in a H_2:H_2O mixture of 12:1. The curve becomes rather steep for cathodic overpotential and shallow under anodic overpotential. This behavior cannot be fitted by the sum of two exponential curves, i.e. by a kind of Butler-Volmer type kinetics. In accordance with Eq. 5, the overpotential affects the oxygen chemical potential or effective partial pressure pO_2^{eff} in the electrode. In line with an ambient-pressure XPS study[34] and the SEM images in Figure 8, metallic Fe nanoparticles are therefore expected at open circuit potential and particularly upon cathodic polarization. Those particles increase the water splitting capability and this probably causes the cathodic current increase. During anodic polarization, the particles become reoxidized and the U-I curve is shallow. The high reproducibility of the ASR and chemical capacitance values during pO_2 or bias cycles at 650°C and the absence of any hysteresis suggest that Fe^0 precipitates mainly in near-surface regions while the bulk remains primarily in the perovskite phase.

However, at 800°C conductivity and ASR measurements become irreproducible in hydrogen rich conditions (not shown) and also SEM images (Figure 8) indicate decomposition of STF37. This supposed decomposition of STF37 at 800°C seems to be in contradiction with the chemical stability observed for STF-GDC composite anodes in 0.97+0.03 bar H_2+H_2O at 800°C.[11] There, however, the electrodes were tested in an electrochemical cell operating at 0.7 V and thus during anodic polarization of the STF electrode. The anodic overpotential increases the chemical potential of oxygen in the anode bulk (or pO_2^{eff}) compared to the atmosphere and stabilizes the perovskite phase. Overall, these results indicate that the exsolution of metallic Fe from STF can strongly increase the electrode kinetics, but only occurs under conditions that are very close to decomposition of the perovskite phase.

Conclusions

The electrochemical properties of $SrTi_{1-x}Fe_xO_{3-\delta}$ thin film electrodes with 30 and 70 mol% Fe were investigated in reducing H_2+H_2O atmosphere at 650°C. Current collectors were applied to the thin film to compensate the relatively low electronic conductivity under reducing conditions. These enabled meaningful electrochemical measurements with homogeneously polarized thin film electrodes and in-plane measurements of electronic and ionic conductivity. In reducing atmosphere, the partial reduction of Fe^{3+} to Fe^{2+} leads to a polaronic electron conduction in the order of 10^{-2} -10^{-1} S/cm, with higher values in more reducing conditions and for higher Fe concentration. The concentration of Fe^{2+} polarons, determined by the chemical capacitance, is in good agreement with literature thermogravimetric data. The ionic conductivities of 0.022 S/cm for STF37 and 0.0035 S/cm for STF73 at 650°C are independent of oxygen partial pressure, which is in line with the expected almost pO_2 independent oxygen vacancy concentration. In H_2/H_2O, STF37 is even a better ion conductor than single crystalline yttria-stabilized zirconia. Higher Fe concentration also decreases the area-specific resistance of the surface reaction and Pt/Ti current collectors on top of STF37 lead to an additional very high TPB activity and can further lower the electrode polarization resistance.

In hydrogen-rich atmospheres or during cathodic polarization, the very low chemical potential of oxygen promotes the formation of catalytically active Fe^0 particles on the surface of STF37, which also decreases the ASR of the electrode. In water-rich atmosphere these particles become oxidized and the ASR increases.[33,34] Hence, the surface reaction mechanism can be switched from oxide-mediated to Fe-metal catalysed by a small variation of the electrode overpotential or gas composition. The exsolution of Fe^0, however, occurs only very close to the thermo-chemical stability limit.

Acknowledgments

The authors gratefully acknowledge funding by the Austrian Science Fund (FWF) projects P4509-N16, W1243-N16, the US NSF fund DMR-1506925, DOE fund DE-NA0002135 and ANPCyT-PICT2013-1032 (Argentina).

References

1. C. Sun, R. Hui, and J. Roller, *J Solid State Electrochem*, **14**(7), 1125 (2009).
2. W. Zhou, R. Ran, and Z. Shao, *J. Power Sources*, **192**(2), 231 (2009).
3. S. B. Adler, *Chemical Reviews*, **104**(10), 4791 (2004).
4. A. Nenning, A. K. Opitz, T. M. Huber, and J. Fleig, *Phys. Chem. Chem. Phys.*, **16**(40), 22321 (2014).
5. S. Tao and J. T. Irvine, *Nat. Mater.*, **2**(5), 320 (2003).
6. S. Tao and J. T. S. Irvine, *J. Electrochem. Soc.*, **151**(2), A252 (2004).
7. X. Yue and J. T. S. Irvine, *Electrochem. Solid-State Lett.*, **15**(3), B31 (2012).
8. S. P. Jiang, L. Zhang, and Y. Zhang, *J. Mater. Chem.*, **17**(25), 2627 (2007).
9. C. Arrivé, T. Delahaye, O. Joubert, and G. Gauthier, *J. Power Sources*, **223**, 341 (2013).
10. A. Atkinson, S. Barnett, R. J. Gorte, J. Irvine, A. J. McEvoy, M. Mogensen, S. C. Singhal, and J. Vohs, *Nat. Mater.*, **3**(1), 17 (2004).
11. S. Cho, D. E. Fowler, E. C. Miller, J. S. Cronin, K. R. Poeppelmeier, and S. A. Barnett, *Energy Environ. Sci.*, **6**(6), 1850 (2013).
12. G. Rupp, A. Limbeck, M. Kubicek, A. Penn, M. Stöger-Pollach, G. Friedbacher, and J. Fleig, *J. Mater. Chem. A*, **2**(19), 7099 (2014).
13. F. Baumann, J. Fleig, G. Cristiani, B. Stuhlhofer, H.-U. Habermeier, and J. Maier, *J. Electrochem. Soc.*, **154**(9), B931 (2007).
14. T. Huber, M. Kubicek, A. Opitz, and J. Fleig, *J. Electrochem. Soc.*, **162**(3), F229 (2015).
15. A. K. Opitz, M. Kubicek, S. Huber, T. Huber, G. Holzlechner, H. Hutter, and J. Fleig, *J. Mater. Res.*, **28**(16), 2085 (2013).
16. J. Fleig, F. S. Baumann, V. Brichzin, H. R. Kim, J. Jamnik, G. Cristiani, H. U. Habermeier, and J. Maier, *Fuel Cells*, **6**(3-4), 284 (2006).
17. W. C. Jung and H. L. Tuller, *Adv. Energy Mater.*, **1**(6), 1184 (2011).
18. Y. Chen, W. Jung, Z. Cai, J. J. Kim, H. L. Tuller, and B. Yildiz, *Energy Environ. Sci.*, **5**(7), 7979 (2012).
19. W. C. Chueh, W. Lai, and S. M. Haile, *Solid State Ionics*, **179**(21), 1036 (2008).
20. Z. A. Feng, F. El Gabaly, X. Ye, Z.-X. Shen, and W. C. Chueh, *Nat. Commun.*, **5**, (2014).
21. S. C. DeCaluwe, M. E. Grass, C. Zhang, F. E. Gabaly, H. Bluhm, Z. Liu, G. S. Jackson, A. H. McDaniel, K. F. McCarty, and R. L. Farrow, *J. Phys. Chem. C*, **114**(46), 19853 (2010).
22. C. Zhang, Y. Yu, M. E. Grass, C. Dejoie, W. Ding, K. Gaskell, N. Jabeen, Y. P. Hong, A. Shavorskiy, and H. Bluhm, *J. Am. Chem. Soc.*, **135**(31), 11572 (2013).
23. W. Lai and S. M. Haile, *J. Am. Ceram. Soc.*, **88**(11), 2979 (2005).
24. W. C. Chueh, Y. Hao, W. Jung, and S. M. Haile, *Nat Mater*, **11**(2), 155 (2012).
25. S. Kogler, A. Nenning, G. M. Rupp, A. K. Opitz, and J. Fleig, *J. Electrochem. Soc.*, **162**(3), F317 (2015).
26. A. Nenning, E. Navickas, P. Velicsanyi, A. K. Opitz, H. Hutter, and J. Fleig, *Solid State Ionics*, **273**, 25 (2015).
27. W. C. Jung and H. L. Tuller, *Solid State Ionics*, **180**(11), 843 (2009).
28. W. C. Jung and H. L. Tuller, *J. Electrochem. Soc.*, **155**(11), B1194 (2008).
29. R. Merkle and J. Maier, *Phys. Chem. Chem. Phys.*, **4**(17), 4140 (2002).
30. S. Steinsvik, R. Bugge, J. Gjønnes, J. Taftø, and T. Norby, *J. Phys. Chem. Solids*, **58**(6), 969 (1997).
31. A. Rothschild, S. J. Litzelman, H. L. Tuller, W. Menesklou, T. Schneider, and E. Ivers-Tiffée, *Sens. Actuators, B*, **108**(1), 223 (2005).
32. A. Rothschild, W. Menesklou, H. L. Tuller, and E. Ivers-Tiffée, *Chem. Mater.*, **18**(16), 3651 (2006).
33. A. K. Opitz, A. Nenning, C. Rameshan, R. Rameshan, R. Blume, M. Hävecker, A. Knop-Gericke, G. Rupprechter, J. Fleig, and B. Klötzer, *Angew. Chem., Int. Ed.*, **54**(9), 2628 (2014).
34. A. Nenning, A. Opitz, C. Rameshan, R. Rameshan, R. Blume, M. Hävecker, A. Knop-Gericke, G. Rupprechter, B. Klötzer, and J. Fleig, *J. Phys. Chem. C*, **120**(3) 1461 (2016).
35. T. Huber, A. Opitz, M. Kubicek, H. Hutter, and J. Fleig, *Solid State Ionics*, **268**, 82 (2014).
36. A. Caneiro, P. Bavdaz, J. Fouletier, and J. Abriata, *Rev. Sci. Instrum.*, **53**(7), 1072 (1982).
37. M. Kuhn, S. Hashimoto, K. Sato, K. Yashiro, and J. Mizusaki, *Solid State Ionics*, **195**(1), 7 (2011).
38. M. Kuhn, J. J. Kim, S. R. Bishop, and H. L. Tuller, *Chem. Mater.*, **25**(15), 2970 (2013).
39. W. C. Chueh and S. M. Haile, *Phys. Chem. Chem. Phys.*, **11**(37), 8144 (2009).
40. Y. Yao, T. Xie, and Y. Gao, *Science* and Technology Press, Shanghai, 677 (1985).
41. M. Filal, C. Petot, M. Mokchah, C. Chateau, and J. Carpentier, *Solid State Ionics*, **80**(1), 27 (1995).
42. M. Dudek, M. Mosiałek, G. Mordarski, R. Socha, and A. Rapacz-Kmita, *Arch. Metall. Mater.*, **56**(4), 1249 (2011).
43. R. A. De Souza, V. Metlenko, D. Park, and T. E. Weirich, *Phys. Rev. B*, **85**(17), 174109 (2012).
44. A. K. Opitz, A. Lutz, M. Kubicek, F. Kubel, H. Hutter, and J. Fleig, *Electrochim. Acta*, **56**(27), 9727 (2011).
45. W. G. Bessler, M. Vogler, H. Störmer, D. Gerthsen, A. Utz, A. Weber, and E. Ivers-Tiffée, *Phys. Chem. Chem. Phys.*, **12**(42), 13888 (2010).
46. A. Nenning, E. Navickas, H. Hutter, and J. Fleig, *J. Phys. Chem. Lett.*, **7**(14), 2826 (2016).
47. T. Zhu, D. E. Fowler, K. R. Poeppelmeier, M. Han, and S. A. Barnett, *J. Electrochem. Soc.*, **163**(8), F952 (2016).
48. H. Zhu, R. J. Kee, V. M. Janardhanan, O. Deutschmann, and D. G. Goodwin, *J. Electrochem. Soc.*, **152**(12), A2427 (2005).
49. P. Velicsanyi, M. Gerstl, A. Nenning, H. Hutter, J. Fleig, and A. Opitz, *ECS Trans.*, **68**(1), 1509 (2015).
50. W. Jung, J. O. Dereux, W. C. Chueh, Y. Hao, and S. M. Haile, *Energy Environ. Sci.*, **5**(9), 8682 (2012).
51. J. Fleig, *Annual Review of Materials Research*, **33**(1), 361 (2003).
52. L. Navarro, F. Marques, and J. Frade, *J. Electrochem. Soc.*, **144**(1), 267 (1997).
53. H. Tuller and A. Nowick, *J. Phys. Chem. Solids*, **38**(8), 859 (1977).
54. S. Wang, T. Kobayashi, M. Dokiya, and T. Hashimoto, *J. Electrochem. Soc.*, **147**(10), 3606 (2000).
55. D. Neagu, G. Tsekouras, D. N. Miller, H. Ménard, and J. T. S. Irvine, *Nat Chem*, **5**(11), 916 (2013).
56. T.-S. Oh, E. K. Rahani, D. Neagu, J. T. Irvine, V. B. Shenoy, R. J. Gorte, and J. M. Vohs, *J. Phys. Chem. Lett.*, **6**, 5106 (2015).
57. D. E. Fowler, A. C. Messner, E. C. Miller, B. W. Slone, S. A. Barnett, and K. R. Poeppelmeier, *Chem. Mater.*, **27**(10), 3683 (2015).
58. D. M. Bierschenk, E. Potter-Nelson, C. Hoel, Y. Liao, L. Marks, K. R. Poeppelmeier, and S. A. Barnett, *J. Power Sources*, **196**(6), 3089 (2011).
59. W. Kobsiriphat, B. D. Madsen, Y. Wang, M. Shah, L. D. Marks, and S. A. Barnett, *J. Electrochem. Soc.*, **157**(2), B279 (2010).
60. V. Y. Zenou, D. E. Fowler, R. Gautier, S. A. Barnett, K. R. Poeppelmeier, and L. D. Marks, *Solid State Ionics*, **296**, 90 (2016).
61. L. Adijanto, V. B. Padmanabhan, R. J. Gorte, and J. M. Vohs, *J. Electrochem. Soc.*, **159**(11), F751 (2012).